

Slow Evolution of Zonal Jets on the Beta Plane

A. J. MANFROI AND W. R. YOUNG

Scripps Institution of Oceanography, University of California, San Diego, La Jolla, California

(Manuscript received 24 July 1997, in final form 5 May 1998)

ABSTRACT

The authors study the stability of a barotropic sinusoidal meridional flow on a β plane. Because of bottom drag and lateral viscosity, the system is dissipative and forcing maintains a basic-state velocity that carries fluid across the planetary vorticity contours; this is a simple model of forced potential vorticity mixing. When the Reynolds number is slightly above the stability threshold, a perturbation expansion can be used to obtain an amplitude equation for the most unstable disturbances. These instabilities are zonal flows with a much larger length scale than that of the basic state.

Numerical and analytic considerations show that random initial perturbations rapidly reorganize into a set of fast and narrow eastward jets separated by slower and broader regions of westward flow. There then follows a much slower adjustment of the jets, involving gradual meridional migration and merger. Because of the existence of a Lyapunov functional for the dynamics, this one-dimensional inverse cascade ultimately settles into a steady solution.

For a fixed β , the meridional separation of the eastward jets depends on the bottom drag. When the bottom drag is zero, the process of jet merger proceeds very slowly to completion until only one jet is left in the domain. For small bottom drag, the steady-state meridional separation of the jets varies as $(\text{bottom drag})^{-1/3}$. Varying the nondimensional β parameter can change the instability from supercritical (when β is small) to subcritical (when β is larger). Thus, the system has a rich phenomenology involving multiple stable solutions, hysteretic transitions, and so on.

1. Introduction

The inverse cascade, or negative viscosity, is a characteristic feature of two-dimensional turbulence. Our interest here is the arrest of this cascade on a β plane by the spontaneous formation of zonal jets. The early turbulence simulations of Rhines (1975) and Williams (1978) showed that the β effect prevents large meridional (i.e., “cross- β ”) fluid excursions. Instead, zonally elongated, persistent flows extend unimpeded across the computational domain. An important and realistic feature of these anisotropic velocity fields is that there is also a strong asymmetry between eastward and westward flow: there are narrow eastward jets separated by broader regions of slower westward flow. This effect is particularly striking in the simulations of baroclinic turbulence reported by Panetta (1993) [see also the review by Rhines (1994)].

Another interesting feature of Panetta’s simulations is that, although arising from active baroclinic turbulence, these zonal jets have an “almost barotropic”

character. It seems plausible that the baroclinic eddies are effectively a random, small-scale forcing for the barotropic mode (as envisaged by Salmon 1980 and Williams 1978). Recently, several investigators have taken this approach either on a β plane (Vallis and Maltrud 1993) or on a sphere (Nozawa and Yoden 1997; Huang and Robinson 1998). A remarkable aspect of the simulations in these three papers is that the large-scale jets are virtually steady even though the system is forced stochastically at small scales. Huang and Robinson emphasize another equally remarkable fact: the energy transfer from the small-scale forcing to the jets is spectrally nonlocal; there is no evidence of a local upscale energy cascade in wavenumber space.

In this article we prescribe deterministic small-scale forcing, which drives a steady sinusoidal shear in the meridional direction, and view the problem as one of weakly nonlinear hydrodynamic stability rather than turbulence phenomenology.

An analytic path is provided by studying the nonlinear evolution of the first instabilities that develop on this small-scale flow as the Reynolds number is increased. Nepomnyashchy (1976) and Sivashinsky (1985) realized that these instabilities have a much larger length scale than that of the forced sinusoidal flow; the nonlocal energy transfer reported by Huang and Robinson (1998) is equivalent to this scale separation. Indeed, Sivash-

Corresponding author address: A. J. Manfroi, Scripps Institution of Oceanography, University of California, San Diego, La Jolla, CA 92093-0230.

E-mail: amanfroi@ucsd.edu

insky's expansion accesses an interesting nonlinear regime because it is primarily based on scale separation rather than on weak nonlinearity.

We follow this path, incorporating three additional features of geophysical interest: the β effect, a uniform mean flow, and bottom drag. The special case in which the basic sinusoidal flow is a stationary (but inviscid) Rossby wave has been studied by Lorenz (1972) and Gill (1974). The inclusion of viscosity makes the problem easier because one can control the instability by operating just past the stability boundary with a slightly supercritical Reynolds number.

The studies by Vallis and Maltrud (1993), Nozawa and Yoden (1997), and Huang and Robinson (1998) all use stochastic forcing, while in our model the forcing is deterministic and steady. The advantage of the deterministic approach is that many aspects of the problem are captured by a tractable and mechanistic model. We show how large-scale instabilities lead to the formation of slowly evolving zonal jets, which are similar to those observed in the turbulence simulations described above and in a number of geophysical circumstances. Specifically, there are narrow and fast eastward jets separated by broader and slower regions of westward flow. We also stress the importance of the bottom drag in the ultimate selection of the spatial scale of the zonal jets. With no bottom friction, the zonal jets very slowly migrate and merge until only one eastward jet remains in the domain of integration. This scale increase is a type of "one-dimensional" inverse cascade. With nonzero bottom drag, the scale increase is arrested and the typical distance between eastward jets of this asymptotic state is proportional to $(\text{bottom drag})^{-1/3}$.

In section 2 we introduce the analytical model and derive the amplitude equation for the leading order perturbation. In section 3 we obtain analytical results for zonally uniform solutions of the amplitude equations. Through various numerical computations we study the formation and evolution of zonal flows in section 4. Section 5 is a discussion of the results and their generality.

2. The amplitude equation

Consider a β plane on which the planetary vorticity distribution is

$$\beta(\sin\alpha x + \cos\alpha y). \quad (2.1)$$

Suppose that a base-state flow with streamfunction Ψ and velocity components $(-\Psi_y, \Psi_x)$ given by

$$(\Psi, -\Psi_y, \Psi_x) = (-Uy - \Psi_0 \cos mx, U, m\Psi_0 \sin mx) \quad (2.2)$$

is driven by arranging suitable forcing. The unconventional rotation of the coordinate system in (2.1) has been taken so that the expression of the velocity in (2.2) is simple.

If $(U, \alpha) = (0, 0)$, then the forcing is pushing the fluid across the planetary vorticity contours. One can visualize this as small-scale deterministic stirring that is mixing planetary potential vorticity. Our focus will be on the special case $\alpha = 0$, in which the planetary vorticity contours run east–west, and the base-state flow in (2.2) is a stationary Rossby wave. This is the problem studied by Lorenz (1972) and Gill (1974).

Frisch et al. (1996) have recently studied the case in which the sinusoidal part of the base-state flow is parallel to the planetary vorticity contours (i.e., $\alpha = \pi/2$ and $U = 0$). In the derivation of Frisch et al., the β effect introduces only minor modifications to the method of Nepomnyashchy (1976) and Sivashinsky (1985). It turns out that the case considered here, in which α is small, both encompasses the final result of Frisch et al. as a limit and demands some nontrivial modifications of the method of Nepomnyashchy (1976) and Sivashinsky (1985).

We write the total streamfunction as $\Psi(x, y) + \psi(x, y, t)$. Introducing nondimensional variables (e.g., $\psi_{\text{dim}} = \nu\psi_{\text{nondim}}$, where ν is the viscosity) gives the following nondimensional equation for the disturbance streamfunction:

$$\nabla^2\psi_t + U\nabla^2\psi_x + R \sin x [\nabla^2\psi_y + \psi_y] + J(\psi, \nabla^2\psi) + \beta \cos\alpha\psi_x - \beta \sin\alpha\psi_y = \nabla^4\psi - \mu\nabla^2\psi, \quad (2.3)$$

where $R \equiv \Psi_0/\nu$ is the Reynolds number of the basic state. The boundary condition on (2.3) is periodicity in both x and y .

The advection term involving U in (2.3) cannot be removed by a change of reference frame because the sinusoidal forcing breaks the Galilean invariance of the barotropic potential vorticity equation. That is, (2.3) is written in the unique reference frame in which the sinusoidal pattern is stationary. Indeed, we show below that the net advection U has many of the same consequences as the β effect. [One can anticipate the equivalence of the two processes by noting that both U and β break the $(x, \psi) \rightarrow (\pi - x, -\psi)$ symmetry of (2.3).]

We now reduce (2.3) following Nepomnyashchy (1976) and Sivashinsky (1985). The key simplification is that the Reynolds number is assumed to be slightly supercritical:

$$R = R_c(1 + \epsilon^2). \quad (2.4)$$

Here, R_c is the critical Reynolds number and the small parameter ϵ controls the strength of the supercriticality. We introduce the following relations:

$$\begin{aligned} \eta &= \epsilon y, & \tau &= \epsilon^4 t, & \mu &= \epsilon^4 \mu_4, \\ \alpha &= \epsilon^5 \alpha_5, & \xi &= \epsilon^6 x, \end{aligned} \quad (2.5)$$

with the corresponding multiscale expansion. From the linear stability analysis of a sinusoidal shear flow (Meshalkin and Sinai 1961; Nepomnyashchy 1976) it is known that, if the difference between the Reynolds

number and the critical Reynolds number is of order ϵ^2 , then the band of unstable wavenumbers has a width of order ϵ and is centered at $k = 0$. This motivates our definition of η . The same linear considerations show that the growth rate of the instability is proportional to $(R - R_c)k^2$, that is, of order ϵ^4 . This justifies our choice of the timescale in (2.5). The other scalings are chosen so that the maximum number of physical processes (e.g., β effect and bottom drag) appear also in the final amplitude equation for the perturbation. We require for now that μ_4 and α_5 are $O(1)$ as $\epsilon \rightarrow 0$. It turns out that we will also have to expand U and β in powers of ϵ :

$$\begin{aligned} U &= U_0 + \epsilon U_1 + \epsilon^2 U_2 + \dots \\ \beta &= \beta_0 + \epsilon \beta_1 + \epsilon^2 \beta_2 + \dots \end{aligned} \quad (2.6a, b)$$

The connections between R_c , U_0 , β_0 , etc., will be determined as the expansion unfolds.

Although our itinerary largely follows that of Sivashinsky, there are some interesting differences in the scenery, including the appearance of a subcritical transition. We sketch the development and relegate the details to appendix A.

One substitutes $\psi = \psi_0 + \epsilon \psi_1 + \dots$ into (2.3) and collects powers of ϵ . It is important to note that the leading term ψ_0 is not small relative to the basic-state streamfunction Ψ_0 . The expansion works because of the spatial-scale separation of the basic flow from the perturbation.

The leading order terms of (2.3) are

$$\mathcal{L}\psi_0 = 0, \quad (2.7a)$$

where \mathcal{L} is the differential operator defined by

$$\mathcal{L}f = f_{xxxx} - U_0 f_{xxx} - \beta_0 f_x. \quad (2.7b)$$

We solve (2.7) by taking

$$\psi_0 = A(\xi, \eta, \tau). \quad (2.8)$$

That is, the leading order disturbance streamfunction has no dependence on the fast variable x . Physically, ψ_0 is independent of x because viscosity acts effectively on the small length scale of the basic state. In a very large domain, the most robust, or unstable, disturbances will be those that have large length scale so that viscosity is ineffective.

The expansion then proceeds in an obvious way by collecting powers of ϵ . The critical Reynolds number is obtained by using ψ_1 in the averaged potential vorticity equation (A.9). One finds that

$$R_c^2 = 2[1 + (\beta_0 - U_0)^2]. \quad (2.9a)$$

Both the mean flow U_0 and the β effect raise the threshold for linear instability above the well-known $\sqrt{2}$ critical Reynolds number. But the next-order terms, $O(\epsilon^5)$, force one to take

$$U_0 = \beta_0. \quad (2.9b)$$

Thus, we are forced back to $R_c = \sqrt{2}$.

The alternative to (2.9b) is to admit evolution on the relatively fast timescale $\epsilon^3 t$. But the resulting amplitude equation is an ill-posed nonlinear diffusion equation. With these considerations we are glimpsing the possibility of subcritical instability. The parameter restriction in (2.9b) is required to control this subcriticality so that it is described by the amplitude equation in (2.12) below.

If one wants to consider a basic state with $U = 0$ then, because of (2.9b), one must take also $\beta_0 = 0$. It follows from (2.6b) that the first nonzero β term is at order ϵ and so the expansion requires small β . One is also free to take $\beta = 0$, but then $U_0 = 0$ is forced by (2.9b). Consequently, from (2.6a), the large-scale advection must be weak. (Recall that one cannot eliminate this weak U with a transformation of coordinates because the sinusoidal forcing breaks Galilean invariance.)

Although the expansion at first looks more complicated than that of Sivashinsky (1985), because of (2.9b) many of the expressions simplify and the calculation is comparably simple. It is also remarkable that the condition in (2.9b) ensures that the basic state in (2.2) is, to leading order, the stationary Rossby wave whose inviscid stability was considered by Lorenz (1972) and Gill (1974).

With (2.9b), the order ϵ term in the expansion is

$$\psi_1 = \sin x R_c A_\eta. \quad (2.10)$$

We can physically explain the instability by noting that the reconstructed fields are

$$\begin{aligned} \psi &= -\sqrt{2} \cos x + A + \epsilon \sin x \sqrt{2} A_\eta + O(\epsilon^2), \\ &= -\sqrt{2} \cos(x + \epsilon A_\eta) + A + O(\epsilon^2), \end{aligned} \quad (2.11a, b)$$

where we have considered $U = 0$ for clarity. The combination $\cos(x + \epsilon A_\eta)$ in (2.11b) shows that the zonal velocity of the large-scale perturbation, $-A_\eta$, tilts the small-scale eddies and so creates a nonzero Reynolds stress correlation. The tilt is small, of order ϵ , because the viscosity arrests the advective distortion of the small-scale fields. These stresses act to increase the strength of the large-scale flow, and this reinforces the tilting. This argument also indicates the spectrally non-local energy transfers in this instability (cf., Huang and Robinson 1998).

Collecting the terms of $O(\epsilon^6)$ from the averaged potential vorticity equation we finally arrive at

$$\begin{aligned} A_{\eta\eta\tau} + 2A_{\eta\eta\eta\eta} + 3A_{\eta\eta\eta\eta\eta\eta} - [(\beta_1 - U_1 + A_\eta)^2 A_\eta]_{\eta\eta\eta} \\ + \frac{1}{3}(A_\eta^3)_{\eta\eta\eta} + \beta_0 A_\xi - \alpha_5 \beta_0 A_\eta = -\mu_4 A_{\eta\eta}. \end{aligned} \quad (2.12)$$

If $\beta_1 - U_1 = 0$ and $\beta_0 = 0$, then this last equation reduces to the results of Nepomnyashchy (1976) and Sivashinsky (1985). If $\beta_1 - U_1 = 0$ and $\beta_0 \rightarrow 0$, with $\beta_0 \alpha_5$ held fixed, then (2.12) reduces to the result of Frisch et al. (1996).

3. Zonally uniform solutions of the amplitude equation

Now let us consider solutions of (2.12), which are independent of the slow zonal coordinate ξ . We also take $\alpha_5 = 0$, so that (2.12) can be integrated twice with respect to η . We define

$$\gamma \equiv \beta_1 - u_1, \quad r \equiv 2 - \gamma^2, \quad (3.1a,b)$$

and write the resulting simplified equation for the leading order perturbation streamfunction $A(\eta, \tau)$ as

$$\begin{aligned} A_\tau &= -\mu A - rA_{\eta\eta} - 3A_{\eta\eta\eta\eta} + 2\gamma(A_\eta^2)_\eta \\ &+ \frac{2}{3}(A_\eta^3)_\eta, \end{aligned} \quad (3.2)$$

where we have lightened our notation by suppressing the subscript 4 on the bottom drag μ . The problem above is solved with a periodic boundary condition, $A(\eta, \tau) = A(\eta + \Lambda, \tau)$, where Λ is the length of the domain. Because the perturbation streamfunction A is periodic in η , there is no net zonal momentum in the perturbation. There is no loss of generality here because one defines the basic-state flow u in (2.2) so that u contains all of the net zonal momentum. Numerical solutions of (3.2) are presented in section 4. The remainder of this section develops the analytic theory that serves as a guide to numerical exploration of (3.2).

The amplitude equation for the perturbation streamfunction A in (3.2) has a negative viscosity term, $-rA_{\eta\eta}$, and also a stabilizing hyperviscosity, $-3A_{\eta\eta\eta\eta}$. The parameter γ (the effective planetary vorticity gradient) in (3.1a) plays two roles. First, γ raises the critical Reynolds number so that if $\gamma^2 > 2$ (i.e., if $r < 0$, so the viscosity is positive) then $A = 0$ is a linearly stable solution. Second, because of the quadratic term $2\gamma(A_\eta^2)_\eta$, the symmetry $A \rightarrow -A$ is broken. Thus, if $\gamma \neq 0$, then eastward flow ($A_\eta < 0$) is different from westward flow ($A_\eta > 0$).

In (3.1) the effects of the net advection u and β are folded into a single parameter, γ . We can assume without loss of generality that $\gamma > 0$, since in (3.2) the sign of γ can be reversed by $\eta \rightarrow -\eta$.

a. The Lyapunov functional

Following Chapman and Proctor (1980), observe that (3.2) can be written in the form

$$A_\tau = -\frac{\delta V}{\delta A}, \quad (3.3a)$$

where V is the functional:

$$V[A] \equiv \int \left(\frac{1}{6}A_\eta^4 + \frac{2}{3}\gamma A_\eta^3 - \frac{1}{2}rA_\eta^2 + \frac{1}{2}\mu A^2 + \frac{3}{2}A_{\eta\eta}^2 \right) d\eta. \quad (3.3b)$$

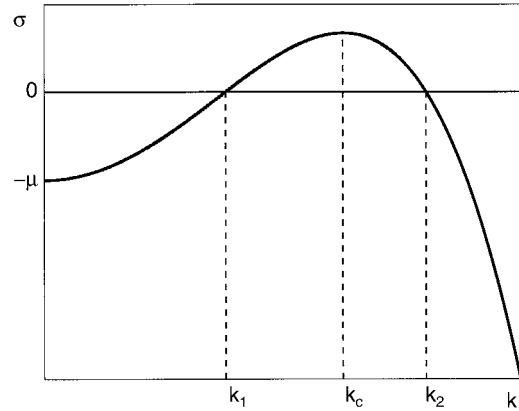


FIG. 1. The linear dispersion relation (3.5a). Wavenumbers between k_1 and k_2 have positive growth rate ($\sigma > 0$) and are unstable. The most unstable wavenumber is $k_c = \sqrt{r/6}$, corresponding to the maximum of σ .

In (3.3b) and subsequent equations, $\int d\eta$ is over one period of the domain, say, $0 < \eta < \Lambda$. Because

$$\frac{dV}{d\tau} = - \int A_\tau^2 d\eta \leq 0, \quad (3.4)$$

the functional V decreases with time in any evolution of the system. Thus, linearly stable, steady solutions of (3.2) correspond to local minima of (3.3b). Further, there can be no sustained time dependence of the system; eventually (3.2) must evolve to a steady state. This conclusion applies only to the zonally uniform (i.e., $A_\xi = 0$) special case of (2.12); we make no claims concerning the stability of these zonally uniform solutions to ξ -dependent perturbations.

b. Linear stability of the trivial solution $A = 0$

The linear stability of the trivial solution $A(\eta, \tau) = 0$ of (3.2) is examined by taking $A(\eta, \tau) \propto \exp(\sigma\tau + ik\eta)$ and neglecting the nonlinear terms. The linear dispersion relation is then

$$\sigma = -3k^4 + rk^2 - \mu. \quad (3.5a)$$

The dispersion relation (3.5a) is shown in Fig. 1; the least stable (or “critical”) wavenumber is at

$$k_c = \sqrt{\frac{r}{6}}. \quad (3.5b)$$

It follows from (3.5a) that a necessary and sufficient condition for the linear instability of $A = 0$ is

$$\mu < \mu_c \equiv \frac{1}{12}(2 - \gamma^2)^2. \quad (3.6)$$

The region of the (γ, μ) plane in which $A = 0$ is linearly unstable is the area below the solid curve $\mu = \mu_c(\gamma)$ in Fig. 2.

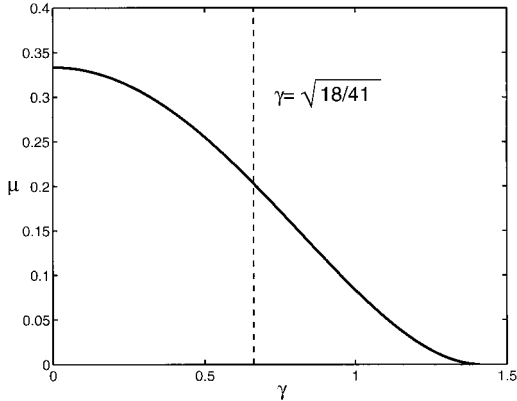


FIG. 2. The area below the solid curve is the region of the (γ, μ) plane in which the trivial solution $A = 0$ is linearly unstable. For $\gamma > \sqrt{18/41}$ the solution $A = 0$ is also nonlinearly unstable (i.e., the Landau coefficient is negative).

c. Weakly nonlinear development of the instabilities

It is instructive to study the weakly nonlinear evolution of the instability found above. It is also convenient to work with the zonally averaged velocity

$$U \equiv -A_\eta. \quad (3.7a)$$

The equation for U can be obtained by differentiating (3.2) once with respect to η and is

$$\begin{aligned} U_\tau = & -\mu U - rU_{\eta\eta} - 3U_{\eta\eta\eta\eta} - 2\gamma(U^2)_{\eta\eta} \\ & + \frac{2}{3}(U^3)_{\eta\eta}. \end{aligned} \quad (3.7b)$$

Suppose that the parameters are adjusted so that the system is just below the solid curve in Fig. 2. That is, the bottom drag coefficient μ is slightly below the critical value in (3.6):

$$\mu = \mu_c - \delta^2 \mu_2, \quad (3.8a)$$

where $\delta \ll 1$ and $\mu_2 \geq 0$ (if μ_2 is negative, the system is linearly stable). Following the standard procedure, we expand U perturbatively as

$$U = \delta U_1 + \delta^2 U_2 + \delta^3 U_3 + \dots \quad (3.8b)$$

and introduce a slow timescale, $T_2 \equiv \delta^2 \tau$. The leading order term for U has the form

$$U_1 = u(T_2) \exp(ik_c \eta) + (\text{c.c.}), \quad (3.9)$$

and the solvability condition at order δ^3 (see appendix B) gives the amplitude equation

$$u_{T_2} = \mu_2 u - \ell |u|^2 u; \quad (3.10a)$$

the Landau coefficient ℓ is an interesting function of γ :

$$\ell(\gamma) \equiv \frac{1}{27}(18 - 41\gamma^2). \quad (3.10b)$$

The main point of interest is that the sign of ℓ changes at $\gamma = \sqrt{18/41} \approx 0.663$. The line $\gamma = \sqrt{18/41}$ is indicated in Fig. 2.

If $\gamma < \sqrt{18/41}$, then ℓ is positive and growth of the linear instability is saturated by weak nonlinearity. If $\gamma > \sqrt{18/41}$, then weak nonlinearity tends to further destabilize the $U = 0$ solution. Negative ℓ also means that there is subcritical instability; even if one is above the solid curve in Fig. 2, where $U = 0$ is linearly stable, a finite-amplitude perturbation can kick U away from zero. Because the amplitude equation (3.2) has a Lyapunov functional, there is no possibility that these subcritical instabilities can “run away.” Thus, (3.2) is a system in which the growth and saturation of subcritical instabilities can be studied.

d. Expansion around the critical point

The Lyapunov functional, $V[A]$ in (3.3), ensures that $U(\eta, \tau)$ cannot grow indefinitely, even if $\ell < 0$; it is just that the saturation is beyond the scope of the approximation in (3.10a). One can capture the saturation of the subcritical instability by expanding around the critical value $\gamma = \sqrt{18/41}$ that we call γ_* . We will set $\gamma = \gamma_* + \delta^2 \gamma_2$ and $\mu \equiv \mu_c - \delta^4 \mu_4$. We need to continue the perturbation expansion for U at the next orders of power of δ and to introduce a new slow timescale $T_4 \equiv \delta^4 \tau$.

From the solvability condition at order δ^5 and from (3.10) we get (see appendix B)

$$u_{T_4} = \mu_4 u + 2.012\gamma_2|u|^2 u - 1.5278|u|^4 u. \quad (3.11)$$

The cubic term in (3.11) is destabilizing when γ_2 is positive, that is, when $\gamma > \gamma_*$. However the fifth-power term is always stabilizing so that (3.11) captures the saturation of the instability. These results will be used in section 4c.

4. An inverse cascade through merger of zonal jets

a. The case with no bottom drag: $\mu = 0$

We begin by considering the case where there is no bottom friction (i.e., $\mu = 0$). It is convenient to work with the zonal velocity U defined in (3.7a). With $\mu = 0$, the evolution equation for U is

$$U_\tau = -rU_{\eta\eta} - 3U_{\eta\eta\eta\eta} - 2\gamma(U^2)_{\eta\eta} + \frac{2}{3}(U^3)_{\eta\eta}. \quad (4.1)$$

We integrate (4.1) using a pseudospectral code with an Adams–Bashforth time-stepping scheme. We use 256 grid points for the space coordinate η . The size of the domain of integration is $\Lambda = 100$, and periodic boundary conditions are imposed [i.e., $U(\eta) = U(\eta + \Lambda)$].

Figure 3 shows the profile of zonal velocity U at different times with $\gamma = 1$. The initial condition is composed of randomly chosen low wavenumber modes. There is a rapid reorganization of the initial condition so that by $\tau = 100$, U consists of strong eastward jets ($U > 0$) separated by broader regions of westward flow ($U < 0$).

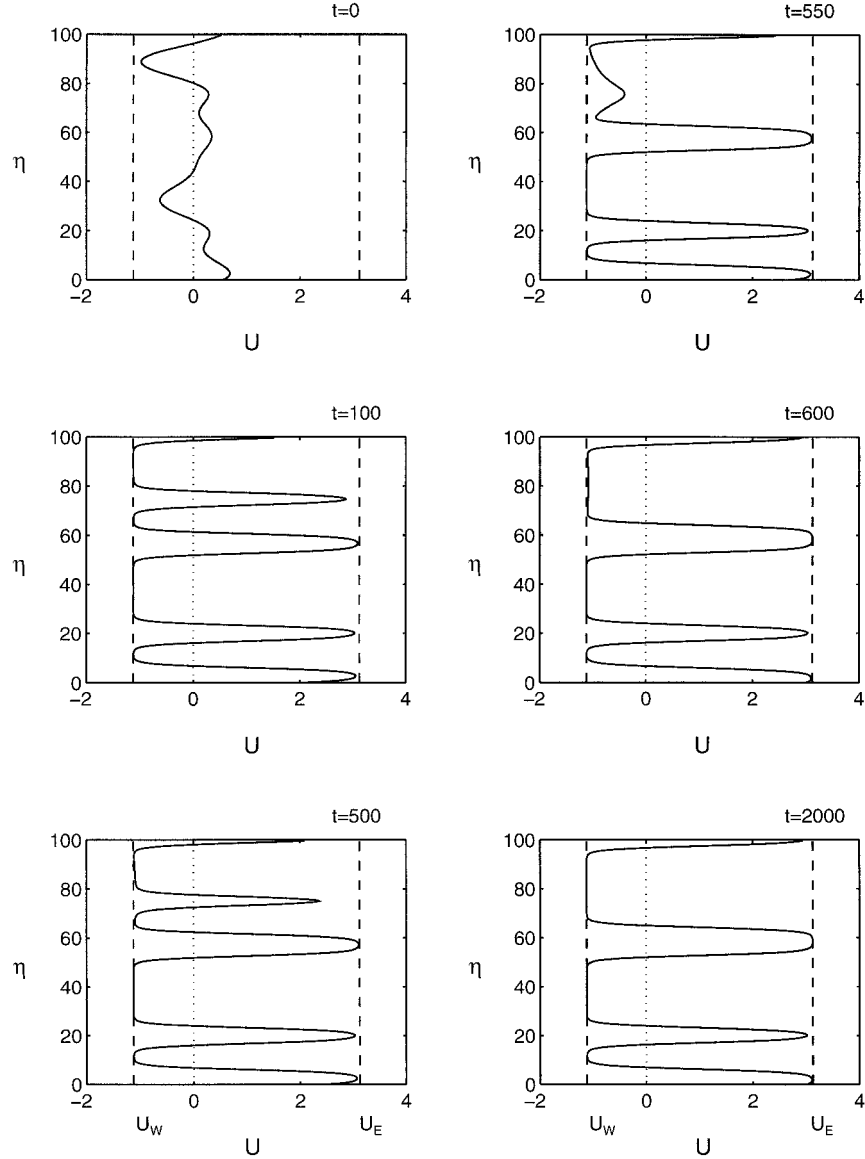


FIG. 3. The zonal velocity $U = -A_\eta$ at six different times indicated near the upper right-hand corner of each panel. U is obtained by numerically integrating (4.1) with periodic boundary conditions. The domain size Λ is 100 and $\gamma = 1$. U_E and U_W , calculated from (4.6), are indicated by the vertical lines in each panel.

($U < 0$). This structure ensures that the net zonal momentum of the perturbation is zero at all times, that is,

$$\int U(\eta, \tau) d\eta = 0. \quad (4.2)$$

The solution in Fig. 3 tends to increase its dominant length scale. This inverse cascade occurs by the successive mergers of westward flow regions with the absorption of the eastward jet that separates them. An example of this can clearly be seen between $\tau = 500$ and $\tau = 600$. The next eastward jet that will be absorbed is the one centered at around $\eta = 20$. This is an in-

creasingly slow process because the eastward jets interact through exponentially small tails. So, the larger the spacing of the jets, the smaller the interaction and the longer it will take for the next merger. In Fig. 3, it is very difficult to notice that the jet centered around $\eta = 20$ has indeed decreased in size between $\tau = 600$ and $\tau = 2000$. Figure 4a is in this respect more clear: it shows the time evolution of U as a contour plot in the (τ, η) plane. In this figure one can also clearly see the disappearance of the jet centered around $\eta = 75$ at times between $\tau = 500$ and $\tau = 600$.

The jet merger process in Figs. 3 and 4 can be understood as the means by which the flow reduces the

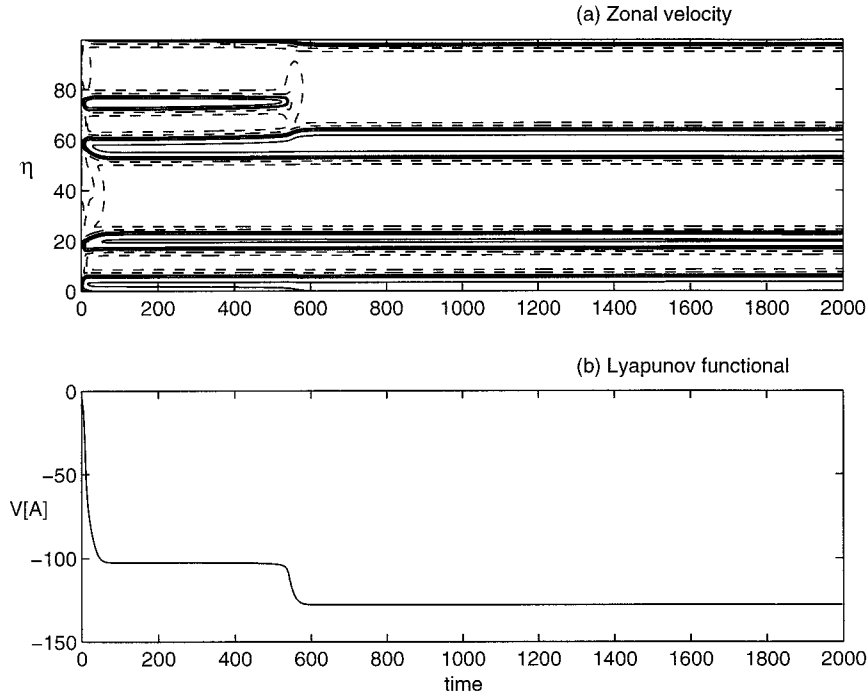


FIG. 4. (a) The history of the solution shown in Fig. 3; contours of constant zonal velocity U in the (τ, η) plane. (b) The evolution of the Lyapunov functional. The sudden drop near $\tau = 550$ corresponds to the elimination of an eastward jet.

Lyapunov functional $V[U]$ in (3.3b). In terms of U , with $\mu = 0$, this functional can be written as

$$V[U] = \int W(U) d\eta + \frac{3}{2} \int U_\eta^2 d\eta, \quad (4.3)$$

where $W(U)$ is a potential function¹

$$W(U) = \frac{1}{6} U^4 - \frac{2}{3} \gamma U^3 - \frac{1}{2} r U^2 - C U. \quad (4.4)$$

Figure 4b shows the time evolution of $V[U]$. As expected from (3.4), the functional is always decreasing. Initially, the value of the functional drops rapidly as the four jets are formed from the random initial condition. The functional $V[U]$ drops again at around $\tau = 550$, corresponding to the disappearance of an eastward jet and an increase of average length scale of the flow, L , defined as the average spacing between eastward jets.

During these merger events, the final term in (4.3) is greatly reduced because two jet boundaries with large shear, $U_\eta \gg 1$, are eliminated. Intuitively, one can view the final term in (4.3) as a penalty associated with having a boundary or interface between eastward and westward flow. By merging jets and eliminating these shear zones,

one is reducing this penalty. The best that one can do in this respect, while observing the momentum constraint in (4.2), is to produce one contiguous region of eastward flow (bounded by two shear zones) in each period; that is the ultimate state, with one eastward jet, toward which the solution in Figs. 3 and 4 is very slowly heading.

The function $W(U)$ has two minima at values of U that we call $U_E > 0$ and $U_W < 0$ (see Fig. 5). To reduce

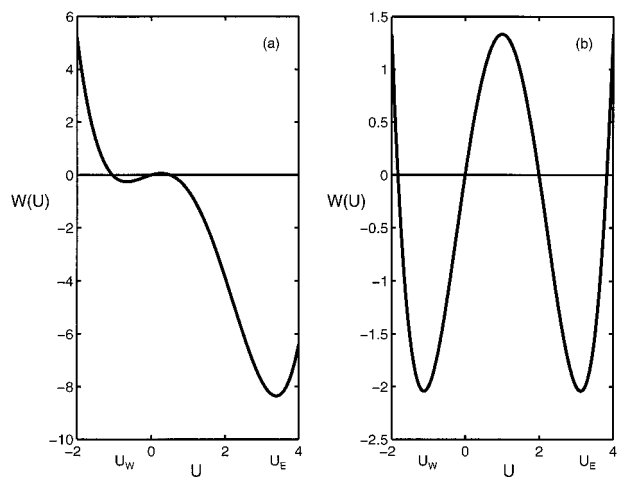


FIG. 5. The potential $W(U)$ must adjust so that the two wells at U_E and U_W have equal depths [as in (b)]. This fixes the value of C as in (4.5). In (a) the value of C is zero.

¹ We have also included an extra term, $CU(\eta, \tau)$, in (4.4); the constant C is a Lagrange multiplier that is used to enforce the momentum constraint in (4.2). Also, again because of (4.2), CU does not change the value of the functional $V[U]$.

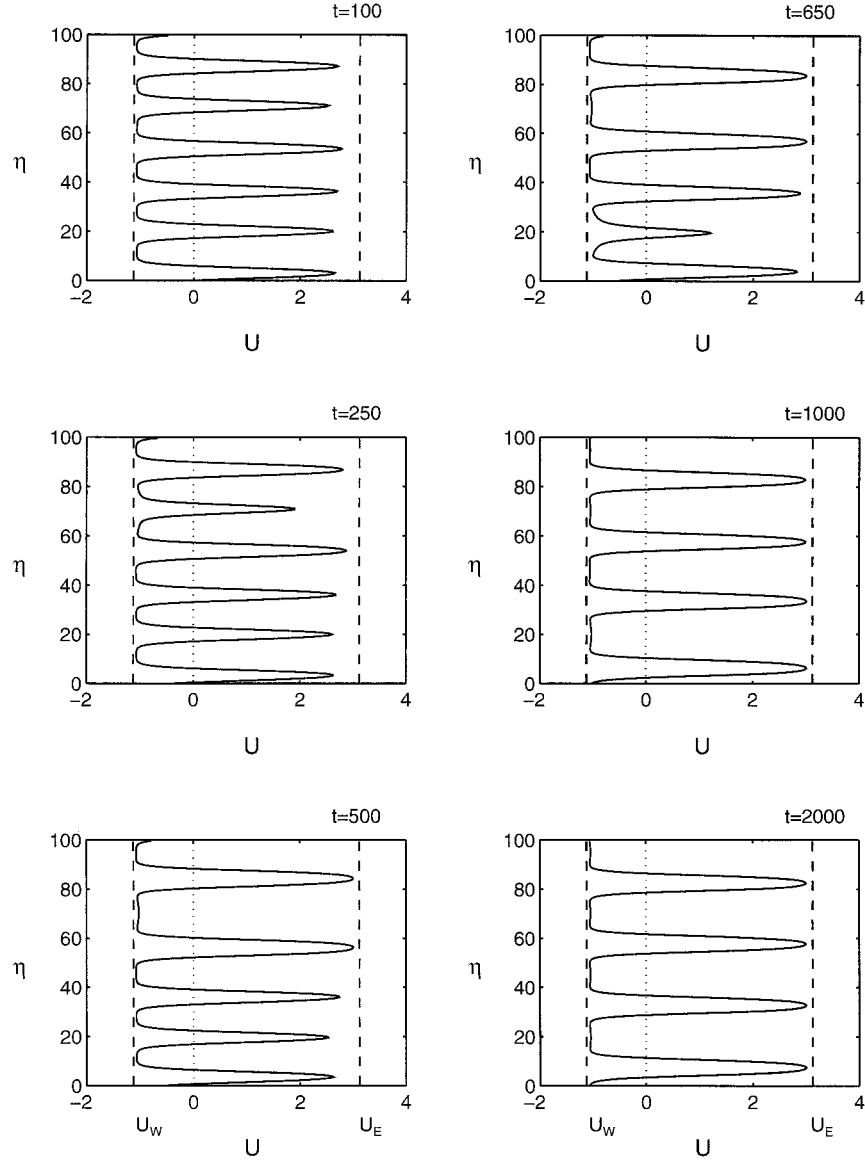


FIG. 6. The zonal velocity U at six different times indicated near the upper right-hand corner of each panel. Here, U is obtained by numerical integration of (4.7) with domain size $\Lambda = 100$ and periodic boundary conditions. In this solution $\gamma = 1$ and $\mu = 0.01$. The initial condition is similar to the one shown in Fig. 3. In this case the inverse cascade is arrested by bottom drag. The result is a periodically spaced set of eastward jets. Here, U_E and U_W , calculated from (4.6), are indicated by the vertical lines in each panel.

the value of $V[U]$ in (4.3), the zonal velocity U will adjust so that it is equal to U_E or U_W . If the potential looked like the example in Fig. 5a, then $W(U)$ would be minimized by making $U = U_E$ everywhere. But this hypothetical resolution of the minimization problem would not satisfy the momentum constraint (4.2). So, we expect regions of space where U is alternatively equal to U_E and U_W connected by shear zones. But if $W(U_E) \neq W(U_W)$, these shear zones could move so as to favor the value of U for which W has an absolute minimum (i.e., U_E in Fig. 5a). Therefore, in order to

maintain the momentum constraint, it must be that $W(U_E) = W(U_W)$. This condition fixes the value of the constant C in (4.4) so that the two minima of the potential functions $W(U)$ have equal depths (as in Fig. 5b). This requirement leads to

$$C = -\gamma \left(2 + \frac{\gamma^2}{3} \right). \quad (4.5)$$

Given (4.5), it follows that

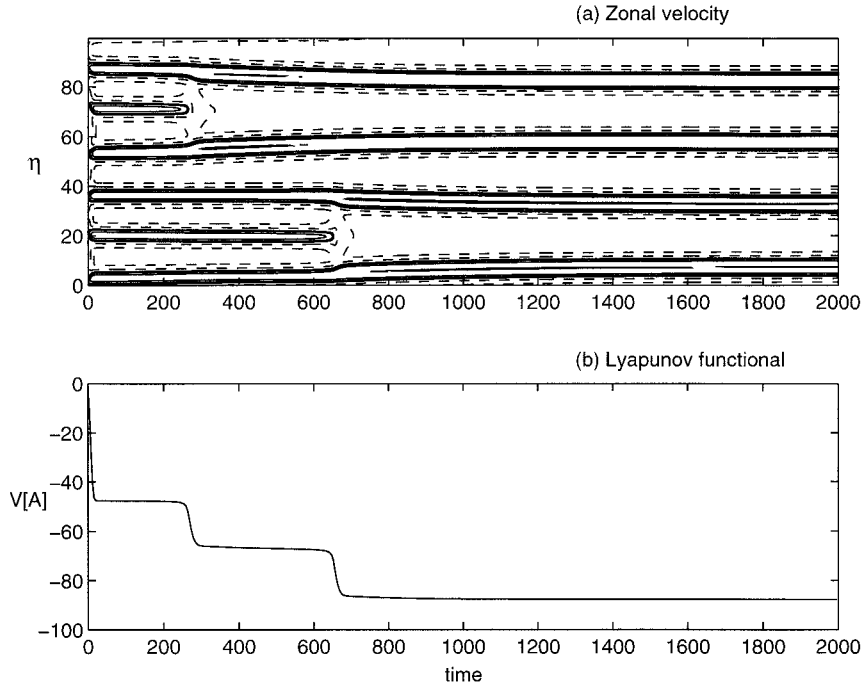


FIG. 7. (a) The complete history of the solution shown in Fig. 6; curves of constant U in the (τ, η) plane. (b) The evolution of the Lyapunov functional. As in Fig. 4, the removal of eastward jets produces sudden drops in the Lyapunov functional.

$$\begin{aligned} U_E &= \gamma + \sqrt{\frac{3}{2}(2 + \gamma^2)}, \\ U_W &= \gamma - \sqrt{\frac{3}{2}(2 + \gamma^2)}. \end{aligned} \quad (4.6a, b)$$

Notice that if $\gamma > 0$, then the eastward zonal flow ($U_E > 0$) is always larger in magnitude than the westward zonal flow ($U_W < 0$). This, in conjunction with the momentum constraint (4.2), explains the pattern in Figs. 3 and 4 of narrow eastward jets alternating with broader and slower regions of westward flow. The values U_E and U_W are indicated by the dashed lines in Fig. 3; there is agreement between (4.6) and the numerical solution of (4.1)².

As remarked by an anonymous reviewer, the substitution $\tilde{U} \equiv U - \gamma$ eliminates the quadratic nonlinearity and so puts (4.1) in the form of a “Cahn–Hilliard equation” with symmetric potential. Then the perturbation schemes developed by Kawasaki and Ohta (1982) and Fraerman et al. (1997) can be used to obtain analytic expressions for the motion of “kinks” (which correspond to the boundaries between easterlies and westerlies in this work).

b. The case with small bottom friction

With nonzero bottom drag, $\mu \neq 0$, the equation for the zonal velocity $U(\eta, \tau)$ is

$$\begin{aligned} U_\tau &= -\mu U - rU_{\eta\eta} - 3U_{\eta\eta\eta\eta} - 2\gamma(U^2)_{\eta\eta} \\ &\quad + \frac{2}{3}(U^3)_{\eta\eta}. \end{aligned} \quad (4.7)$$

Figure 6 shows the profile of zonal velocity $U(\eta, \tau)$ at various times for $\gamma = 1$ and $\mu = 0.01$. For $\tau = 100$ in Fig. 6 it can already be seen that the evolution is different from the one with $\mu = 0$ in Fig. 3. Two cases in which eastward jets disappear can be seen at $\tau \approx 250$ and $\tau \approx 650$. Figure 7a shows a contour plot of $U(\eta, \tau)$ in the (τ, η) plane. The two merger events at $\tau \approx 250$ and $\tau \approx 650$ in Fig. 6 are also evident in Fig. 7a. Figure 7b shows the time evolution of the functional $V[A]$. As expected, $V[A]$ is always decreasing in time and its value drops rapidly every time an eastward jet is absorbed by the merger of two westward flow regions. In Fig. 7a the configuration at $\tau = 1200$ is basically the same as the one at $\tau = 2000$ and later times; the asymptotic state is a periodic solution with four eastward jets in the domain.

In fact, if $\mu \neq 0$, we expect the wavelength (L) of the solution to reach an asymptotic finite value independent of the domain size, Λ , provided that the latter is very large (i.e., if $L \ll \Lambda$). The reason for this can be understood by considering again the functional $V[A]$.

² Notice that if γ is negative, then the eastward flow is wider and slower than the westward flow. This effect might be seen in numerical simulations if one added a net advection u through a field of stationary stochastic forcing.

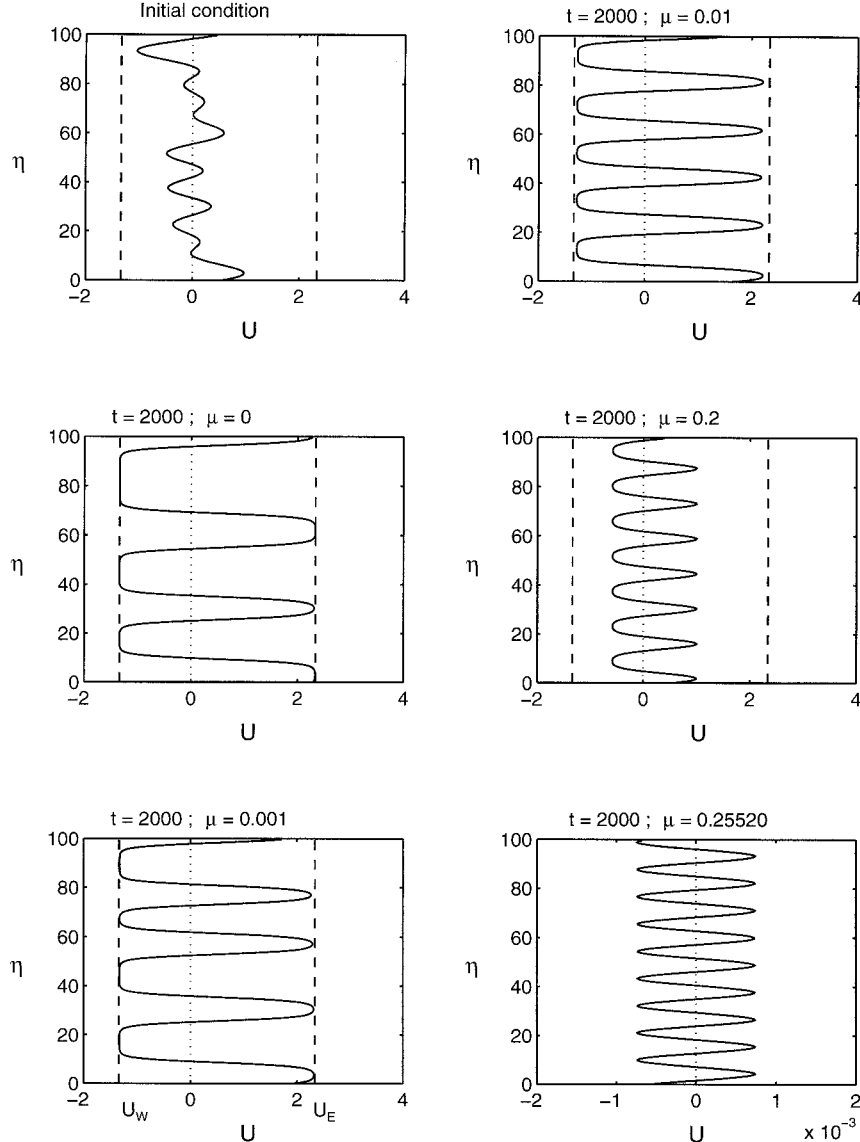


FIG. 8. Five different numerical solutions of (4.7), all with $\gamma = \frac{1}{2}$, and various values of the bottom drag μ indicated at the top of each panel. The upper-left panel is the initial condition. The results at time $\tau = 2000$ are shown in the other five panels. For $\mu = 0$ the inverse cascade is slowly reducing the number of jets (three at $\tau = 2000$ in the middle left panel). As μ is increased, the number of jets increases. Note that the scale for U in the lower-right panel is different from the other panels. In this last panel the value of μ is slightly below the critical value for linear stability so the amplitude of the solution is very small. U_E and U_w , calculated from (4.6), are indicated by the vertical lines in each panel.

For $\mu > 0$ another term needs to be added to the right-hand side of (4.3) so that the functional is now

$$\begin{aligned} V[A] = & \int W(U) d\eta + \frac{3}{2} \int U_\eta^2 d\eta \\ & + \frac{\mu}{2} \int A^2 d\eta. \end{aligned} \quad (4.8)$$

If $\mu > 0$, then the last extra term in (4.8) is always positive. In regions where $U = -A_\eta$ is a nonzero constant, A is

proportional to η . It follows that the integral of A^2 over a period, L , of the solution will be proportional to L^3 . Therefore, if $\mu \neq 0$, the final term in (4.8) is a penalty that increases as the period L of the solution increases.

Indeed, let us rewrite the functional as

$$V[A] = \frac{\Lambda}{L} \left[\int_0^L W(U) d\eta + \int_0^L \frac{3}{2} U_\eta^2 d\eta + \int_0^L \frac{\mu}{2} A^2 d\eta \right], \quad (4.9)$$

so that the integrals in (4.9) are over a period, L , of the solution. To obtain the value of the functional over the domain Λ we need to multiply by the number of wavelengths in the domain, Λ/L . There are three contributions to $V[A]$ from the three integrals in (4.9). The first integral is linear in L , because $W(U)$ is constant for most of the period of the solution. Divided by L this term gives a constant contribution to the functional. The second integral is independent of L because its contribution comes only from the boundary layers where U changes rapidly from the value U_E to U_W and vice versa, and the thickness of these boundaries is independent of L . Divided by L this second term gives a contribution proportional to L^{-1} . The last integral in (4.9) is proportional to L^3 and divided by L gives a contribution proportional to L^2 . If we vary $V[A]$ with respect to L , and minimize, we see that the jet spacing L scales as $\mu^{-1/3}$ when μ is small.

c. The case with “strong” bottom friction

The scaling law $L \propto \mu^{-1/3}$ is difficult to verify numerically because as μ is decreased the adjustment times become very long, and because the domain size Λ eventually intrudes, since in our numerical integrations the condition $L \ll \Lambda$ is not satisfied. However, numerical calculations clearly show that the ultimate spacing of the jets decreases as μ is increased with γ fixed; the story is complicated by the qualitative changes that occur depending on whether γ is fixed at a value for which the instability is supercritical ($\gamma < \sqrt{18/41}$) or a value for which the instability is subcritical ($\gamma > \sqrt{18/41}$). We first discuss the easy case, $\gamma < \sqrt{18/41}$.

Figure 8 shows the profile of the zonal velocity U at $\tau = 2000$ for various runs with $\gamma = 0.5 < \sqrt{18/41}$ and different values of the bottom drag μ . For $\mu = 0$ there is no evident periodicity and, as in Figs. 3 and 4, the solution will tend to a single eastward jet. In Fig. 8 the three cases with $\mu \leq 0.01$ have jets whose amplitude agrees well with the values U_E and U_W in (4.6) (obtained by considering $\mu = 0$).

Increasing the bottom drag μ with $\gamma = 1/2$ in Fig. 2 means that one eventually passes over the stability boundary μ_c in (3.6) (i.e., the solid curve in Fig. 2). For $\gamma = 0.5$, $\mu_c \approx 0.25521$, and Fig. 8 shows how the jets smoothly disappear by reducing their amplitude as $\mu \rightarrow \mu_c$. Indeed, from (3.8a) and (3.8b) we see that the jet amplitude scales as $\sqrt{\mu_c - \mu}$. This is shown schematically in the bifurcation diagram for a supercritical instability in Fig. 9. The analysis in section 3c also shows that as $\mu \rightarrow \mu_c$ the separation of the jets is given by $2\pi/k_c$, where k_c is given by (3.5b). Indeed, the bottom right-hand panel of Fig. 8 shows that for μ near μ_c , the wavelength of the pattern agrees well with $2\pi/k_c$ (for $\gamma = 1/2$, this is $2\pi/k_c \approx 11.63$).

The above results are for a value of γ that is less than the critical value $\gamma_* = \sqrt{18/41}$. When $\gamma > \sqrt{18/41}$ the behavior of the system as a function of μ is more

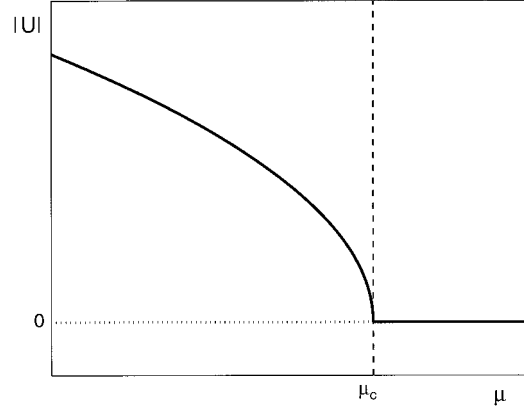


FIG. 9. For μ slightly less than μ_c , the amplitude of the stable solution scales as $\sqrt{\mu_c - \mu}$ and the zero amplitude solution is unstable. When $\mu > \mu_c$ the only stable solution has zero amplitude. In this schematic bifurcation diagram, which applies only to the case $\gamma < \sqrt{18/41}$, a thick, continuous line indicates a linearly stable solution and a dotted line indicates an unstable solution.

complicated because in this case, as shown by (3.11), there is subcritical instability. Figure 10 shows the profile of the zonal velocity U at $\tau = 2000$ for various runs with different values of the bottom drag, but now with $\gamma = 1 > \sqrt{18/41}$. The initial condition is the same as in Fig. 8. Again, both the jet spacing and the jet amplitude decreases as the bottom drag μ increases. But there is a qualitative difference between Figs. 8 and 10. If $\gamma = 1$, then $\mu_c \approx 0.08333$, and one can see in Fig. 10 that even for $\mu > \mu_c$ there is a finite amplitude solution, that is, the jets persist at finite amplitude even when the bottom friction parameter is well above the solid curve in Fig. 2. Thus, in Fig. 10, the linear stability of the solution $U = 0$ is no longer a reliable guide (as it was in Fig. 8).

To understand these results one can consider the bifurcation diagram for a subcritical instability. To do this, let us rewrite (3.11) in a simpler form:

$$u_{T_4} = -m_1 u + m_3 u^3 - m_5 u^5, \quad (4.10)$$

where m_1 , m_3 , and m_5 are positive coefficients related in an obvious way to those in (3.11). For simplicity, we have limited our attention to u real. Following, for example, Thual and Fauve (1988) we consider the potential F defined by

$$F(u) \equiv \frac{1}{2}m_1 u^2 - \frac{1}{4}m_3 u^4 + \frac{1}{6}m_5 u^6. \quad (4.11)$$

Equation (4.10) is equivalent to

$$u_{T_4} = -\frac{\partial F}{\partial u} \quad (4.12a)$$

and also

$$F_{T_4} = -\left(\frac{\partial F}{\partial u}\right)^2 \leq 0. \quad (4.12b)$$

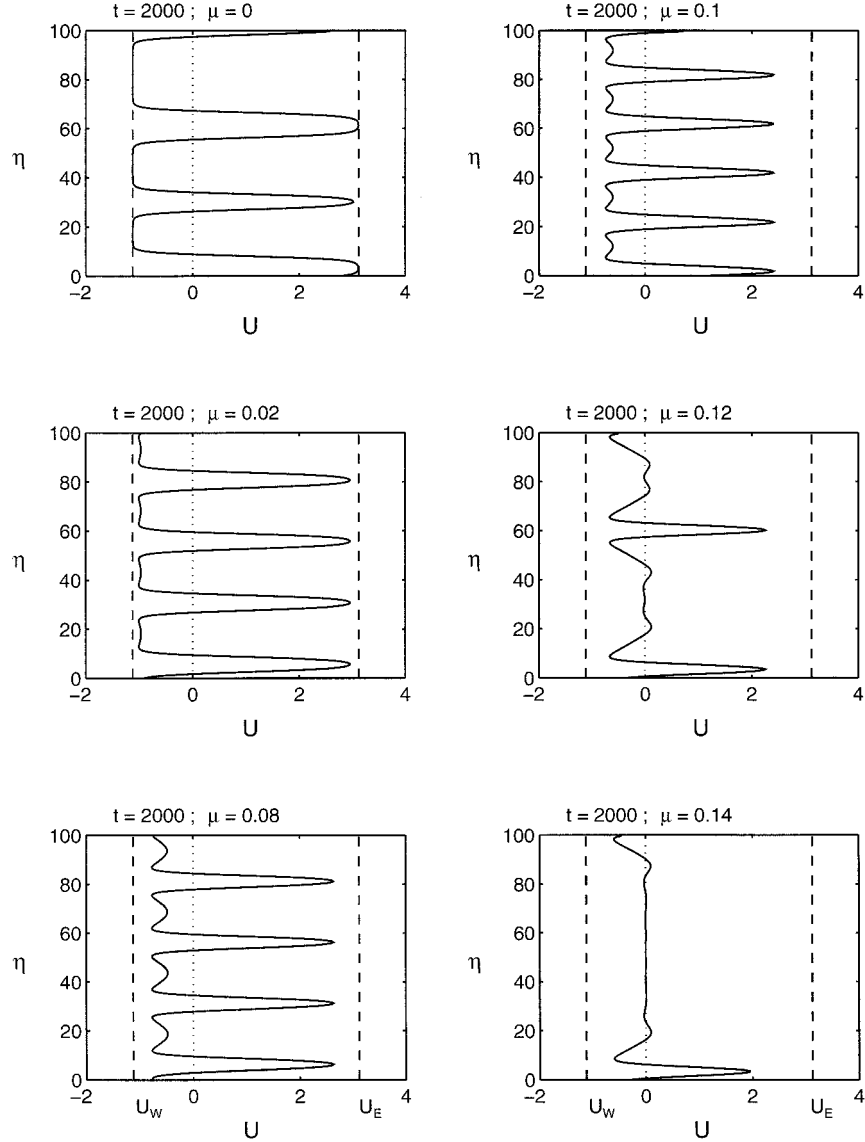


FIG. 10. Six different solutions for $U(\eta, \tau)$ calculated numerically from (4.7), all with $\gamma = 1$ and various values of the bottom drag μ (indicated at the top of each panel) at time $\tau = 2000$. The initial condition is similar to that in Fig. 8. Here, U_E and U_w , calculated from (4.6), are indicated by the vertical lines in each panel.

Equation (4.12) shows that u will evolve such as to minimize $F(u)$. Therefore, a local minimum of $F(u)$ is a stable stationary solution of (4.10), while a local maximum of $F(u)$ is an unstable stationary solution. For a range of values of μ ($\mu_c < \mu < \mu_s$), the potential $F(u)$ has three extrema (see Fig. 11a) and therefore there are three stationary solutions, two of which are linearly stable (the minima in Fig. 11a). The absolute minimum of $F(u)$ corresponds to a globally stable solution, while the other minimum corresponds to a metastable solution. The metastable solution has a larger value of $F(u)$ and so it is less stable than the globally stable solution [the absolute minimum of $F(u)$]. As can be seen in Fig. 11a,

there is a value of μ that we call μ_m for which the two stable solutions exchange roles. For $\mu_c < \mu < \mu_m$ the globally stable solution has finite amplitude ($u \neq 0$) and the metastable one has zero amplitude. For $\mu_m < \mu < \mu_s$ the reverse is true. This behavior is summarized in the bifurcation diagram in Fig. 11b, which also helps us understand the results in Fig. 10.

Even though $\mu_c = 0.08333$, the case with $\mu = 0.1$ in Fig. 10 is not qualitatively different from the one with $\mu = 0.08$. In these cases the finite amplitude solution in Fig. 10 is globally stable (i.e., $\mu_m > 0.1$). For $\mu = 0.12$ and 0.14 the zonal velocity has a pulselike structure with localized regions of eastward and west-

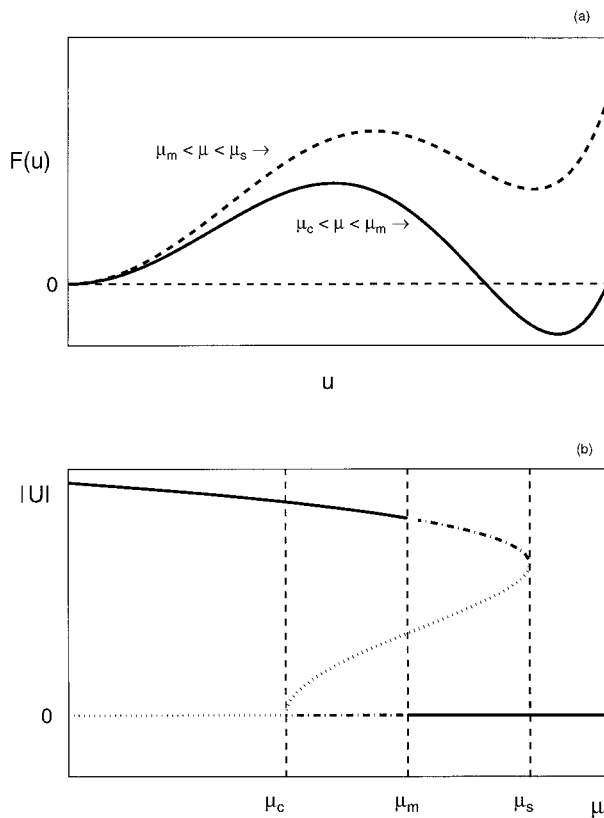


FIG. 11. Bifurcation diagram in the case $\gamma > \sqrt{18/41}$. (a) The potential $F(u)$ has three extrema corresponding to stationary solutions of (3.11). When $\mu_c < \mu < \mu_m$ (the solid curve), the absolute minimum of F is achieved with a finite amplitude solution $u \neq 0$. When $\mu_m < \mu < \mu_s$ (the dashed curve), the trivial solution $u = 0$ is the global minimum; in this case the finite amplitude solution is metastable. (b) The subcritical bifurcation diagram. Globally stable solutions are indicated by a thick solid curve and metastable solutions by a dash-dot line. The unstable solution is dotted. At $\mu = \mu_m$ the trivial solution $u = 0$ and the finite amplitude solution $u \neq 0$ exchange stability properties [i.e., the two minima of $F(u)$ have equal depth].

ward flow separated by regions of zero velocity. Computations show that the number and position of these structures depend on the initial conditions. Therefore, from solutions of the initial value problem it is not obvious if the finite amplitude solution is globally stable or metastable in these cases. An answer is obtained by numerically evaluating the Lyapunov functional in (4.8). The solution $A = 0$ obviously has $V[0] = 0$. So if the finite amplitude solution has $V[A] < 0$, then it is globally stable (i.e., it is more stable than $A = 0$). And if $V[A] > 0$, then the finite amplitude solution is metastable. In Fig. 10, the Lyapunov functional has a negative value for the run with $\mu = 0.12$, which shows that the finite amplitude solution is globally stable. On the other hand, the Lyapunov functional is positive for the run with $\mu = 0.14$, which shows that the finite amplitude solution is metastable in this case. Therefore, for $\gamma = 1$, we have $0.12 < \mu_m < 0.14$. The different sign of the Lyapunov

functional for these two values of μ has been verified by various runs with different initial conditions.

d. Reconstruction of the flow

To this point we have visualized the solution by dealing mostly with the zonal velocity $U = -A_\eta$. However, this is only the first term in the amplitude expansion. It is interesting to reconstruct the two-dimensional field by calculating $\Psi + \psi_0 + \epsilon\psi_1 + \epsilon^2\psi_2 + \epsilon^3\psi_3$ using the expressions for ψ_n in appendix A and with Ψ given by (2.2). The supercriticality parameter ϵ defined in (2.4) does not appear in the amplitude equation. However, in order to reconstruct the total streamfunction in Fig. 12, it is necessary to specify a value of ϵ . We take $\epsilon = 1/2$; this is a tradeoff between a convincingly small ϵ and a value that is large enough to show the main effects of the instability. (If ϵ is too small, the large separation of scale between the zonal and meridional directions gives even narrower zonal oscillations than in Fig. 12.)

Figure 12 shows a case with basic flow $\Psi = -\Psi_0 \cos mx$. Because $U = 0$, the basic state velocity is a pure meridional flow, $V = m\Psi_0 \sin mx$; with no instability this basic state would move fluid steadily northward and southward in alternating bands. The development of the instability in Fig. 12 produces quasi-zonal streamlines. The fast eastward jets and the regions of slow westward flow are clearly visible in the streamfunction. Superimposed on this zonal flow are the oscillations of the basic streamfunction $-\Psi_0 \cos mx$. The superposition of these perpendicular velocities produces the small “cat’s-eye” vortices, which are located within the shear bands that separate westward and eastward flow.

5. Discussion and conclusions

Earlier studies have shown that stochastically forced β plane motion evolves into strong, quasi-steady zonal flows. The goal of the present study has been to develop a mechanistic model of these jets. Because the model in (2.12) involves at least three interesting nondimensional parameters (viz., the effective β parameter, the bottom drag μ , and the domain size Λ), we do not claim to have exhausted this problem even in the special case (3.2) in which there are no zonal variations.

Our approach, which is based on the parametric assumption that the small-scale forcing is only slightly supercritical, cannot access the eddying regime that is the focus of recent works such as Vallis and Maltrud (1993), Nozawa and Yoden (1997), and Huang and Robinson (1998). Yet our results are similar to those found in these earlier studies; our system develops a number of very slowly evolving eastward jets separated by wider regions of westward flow.

Another point of comparison with simulations is that, in the expansion scheme, the relative vorticity

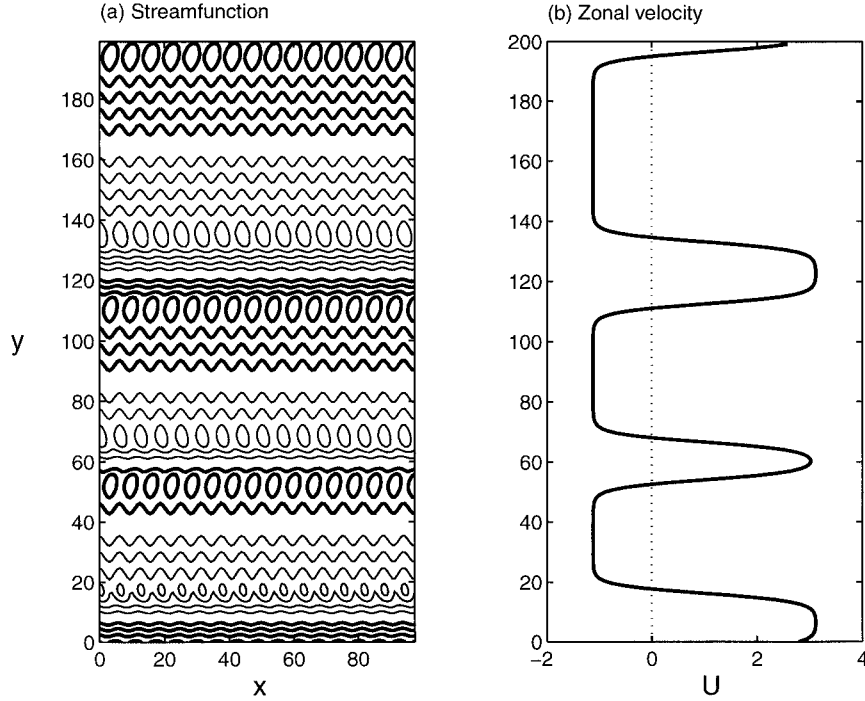


FIG. 12. Results at $\tau = 2000$ for a run with $U_0 = U_1 = \beta_0 = 0$, $\gamma = \beta_1 = 1$, $\mu = 0$, and $\epsilon = \frac{1}{2}$. (a) The streamfunction obtained by adding the first four terms of the perturbation streamfunction to the basic flow streamfunction $\Psi(x)$. Notice the tilted vortices that are localized within the shear bands separating eastward and westward flows. The tilt indicates nonzero Reynolds stresses in these regions and the energy transfer is from the small-scale eddies to the large-scale zonal flow. (b) Profile of the leading order velocity perturbation U , which is used to reconstruct the streamfunction in the left-hand panel. This is the same calculation as the upper-left hand panel of Fig. 10.

gradient of the zonal mean flow is $O(\epsilon^2)$ smaller than the planetary vorticity gradient β . (And so the jets we describe are all strongly stable by the Rayleigh–Kuo condition.) An analogous inequality is characteristic of the numerical simulations referenced above. In all three cases the β effect is stronger than the vorticity gradients of the zonal mean flow. (For instance, Fig. 10 of Vallis and Maltrud shows that \bar{U}_{yy} is, at most, 15% of β .) It is a disappointing failure of the expansion that it does not capture the interesting dynamics that must ensue if the amplitude of the zonal jets is large enough to result in secondary Rayleigh–Kuo instability. As of yet, this regime has not been realized computationally.

One qualitative effect that has not been seen in numerical simulations, but that is strongly suggested by our results, is that jets with the characteristic east–west asymmetry should form if $\beta = 0$ and $U \neq 0$. In this case, the small-scale forcing defines a “stationary” reference frame, and then U is large-scale advection relative to this frame. [Alternatively, if the net advection is eliminated with a Galilean shift, then one has Sivashinsky’s (1985) problem, except that the forcing pattern translates like $\cos(x - Ut)$.]

The very slow evolution of the zonal jets is a problem for direct numerical simulations of the β plane turbulence problem. We are fortunate that there is a Lyapunov

functional that shows that (3.2) is evolving to a steady state, that is, the long time behavior of (3.2) is easily understood. For example, we know in advance that the jets cannot perpetually migrate back and forth across the domain. [Panetta (1993) suggests that this happens in his baroclinic system.] Rather, the final location of a jet in our model is merely an accident of the initial conditions. One is left to wonder how (or if) this variational structure is lost as more physics is systematically included. For instance, we have not been able to obtain a variational principle for the system (2.12), which retains the zonal structure of the perturbation ($A_\xi \neq 0$). And one expects that increasing the Reynolds number of the small-scale forcing will surely result in more interesting β plane–jet dynamics.

Another possibility is that, even if the deterministic part of the dynamics is variational, the small-scale turbulence also provides a fluctuating force that may cause the jets to meander in a Brownian fashion; when the jets are widely separated they interact only through the overlap of exponentially small tails.³ The weak inter-

³ This observation is systematically exploited by the method of Kawasaki and Ohta (1982) and Fraerman et al. (1997); see also the review by Balmforth (1995). These techniques allow one to access the slowly evolving regime with modest computational resources.

action of well-separated jets could be overwhelmed by small noise. This does not seem to be the case in the simulations by Vallis and Maltrud (1993), Nozawa and Yoden (1997), and Huang and Robinson (1998), who observe quasi-steady jets despite the stochastic forcing. In fact, these authors note that the observed jets are steadier when the separation between the forcing scale and the jet scale is larger.

We have also found that bottom drag is important in selecting the spatial separation of the jets in our model. If the bottom drag is zero, then the jets very slowly migrate and merge until only a single region of eastward flow remains in the domain. Increasing the bottom drag arrests this one-dimensional inverse cascade and results in a periodic array of jets; the stronger the bottom drag, the smaller the jet spacing. Because increasing bottom drag also decreases the zonal velocities, weaker zonal flows are associated with smaller jet spacing (e.g., see Fig. 8). However, this is not an endorsement of Rhines's $\sqrt{U_{\text{RMS}}/\beta}$ scaling. Rhines's scale has no utility in the parameter range of our model. For example, in Fig. 8, as the bottom drag is increased to the critical value μ_c the jets smoothly disappear by decreasing their velocity while keeping a fixed wavelength $2\pi/k_c$.

Acknowledgments. We would like to thank Neil Balmforth and Paola Cessi for useful conversations on this problem. This research is supported by the National Science Foundation Grant OCE-9529824.

APPENDIX A

Derivation of the Amplitude Equation

This appendix collects the details of the derivation of the amplitude equation (2.12). To make a self-contained presentation we have repeated some equations from section 2. We suppose that a base state flow of the form

$$(\Psi, -\Psi_y, \Psi_x) = (-uy - \Psi_0 \cos mx, u, m\Psi_0 \sin mx) \quad (\text{A.1})$$

is driven by a suitable forcing on a β plane on which the planetary vorticity distribution is

$$\beta(\sin\alpha x + \cos\alpha y). \quad (\text{A.2})$$

If the total streamfunction is $\Psi(x) + \psi(x, y, t)$ then the disturbance $\psi(x, y, t)$ satisfies the nonlinear equation

$$\begin{aligned} & \nabla^2 \psi_t + u \nabla^2 \psi_x + m \Psi_0 \sin mx [\nabla^2 \psi_y + m^2 \psi_y] \\ & + J(\psi, \nabla^2 \psi) + \beta \cos\alpha \psi_x - \beta \sin\alpha \psi_y \\ & = \nu \nabla^4 \psi - \mu \nabla^2 \psi, \end{aligned} \quad (\text{A.3})$$

for which we consider periodic boundary condition in both x and y .

Introducing the nondimensional variables

$$(\hat{x}, \hat{y}) = (mx, my), \quad \hat{t} = tm^2 \nu, \quad \hat{\psi} = \psi/\nu, \quad (\text{A.4})$$

into (A.3) results in

$$\begin{aligned} & \hat{\nabla}^2 \hat{\psi}_t + \hat{u} \hat{\nabla}^2 \hat{\psi}_x + R \sin \hat{x} [\hat{\nabla}^2 \hat{\psi}_y + \hat{\psi}_y] \\ & + J(\hat{\psi}, \hat{\nabla}^2 \hat{\psi}) + \hat{\beta} \cos \alpha \hat{\psi}_x - \hat{\beta} \sin \alpha \hat{\psi}_y \\ & = \hat{\nabla}^4 \hat{\psi} - \hat{\mu} \hat{\nabla}^2 \hat{\psi}, \end{aligned} \quad (\text{A.5a})$$

where

$$\begin{aligned} R & \equiv \frac{\Psi_0}{\nu}, & \hat{u} & \equiv \frac{u}{m\nu}, \\ \hat{\beta} & \equiv \frac{\beta}{\nu m^3}, & \hat{\mu} & \equiv \frac{\mu}{\nu m^2}. \end{aligned} \quad (\text{A.5b})$$

Here, R is essentially the Reynolds number of the basic state. We now lighten our notation by dropping the decoration on the dimensionless variables.

To study the system slightly above criticality we suppose that

$$R = R_c(1 + \epsilon^2), \quad (\text{A.6a})$$

with R_c the critical Reynolds number and ϵ a small parameter. We also introduce

$$\begin{aligned} \mu & = \epsilon^4 \mu_4, & \alpha & = \alpha_5 \epsilon^5, & \xi & = \epsilon^6 x, \\ \eta & = \epsilon y, & \tau & = \epsilon^4 t & & \end{aligned} \quad (\text{A.6b})$$

with the corresponding multiscale expansions:

$$\partial_x \rightarrow \partial_x + \epsilon^6 \partial_\xi, \quad \partial_y \rightarrow \epsilon \partial_\eta, \quad \partial_t \rightarrow \epsilon^4 \partial_\tau. \quad (\text{A.6c})$$

It is required that μ_4 and α_5 be $O(1)$ as $\epsilon \rightarrow 0$.

Putting (A.6b,c) into (A.5a) gives

$$\begin{aligned} & \epsilon^6 \psi_{x\tau} + \epsilon^6 \psi_{\eta\eta\tau} + u \psi_{xxx} + \epsilon^2 u \psi_{\eta\eta x} + \epsilon^6 u \psi_{xx\xi} \\ & + \epsilon R \sin x [\psi_{xx\eta} + \psi_\eta] + \epsilon^3 R \sin x \psi_{\eta\eta\eta} \\ & + \epsilon (\psi_x \psi_{xx\eta} - \psi_\eta \psi_{xx\eta}) + \epsilon^3 (\psi_x \psi_{\eta\eta\eta} - \psi_\eta \psi_{\eta\eta x}) \\ & + \beta \psi_x + \epsilon^6 \beta \psi_\xi - \epsilon^6 \beta \alpha_5 \psi_\eta \\ & = \psi_{xxxx} + 2\epsilon^2 \psi_{xx\eta\eta} + \epsilon^4 \psi_{\eta\eta\eta\eta} - \epsilon^4 \mu_4 \psi_{xx} \\ & - \epsilon^6 \mu_4 \psi_{\eta\eta} + O(\epsilon^7). \end{aligned} \quad (\text{A.7})$$

Denote an average over the fast scale x by an overbar. For instance,

$$\bar{\psi}(\xi, \eta, \tau) \equiv \frac{1}{2\pi} \int_{-\pi}^{+\pi} \psi(x, \xi, \eta, \tau) dx. \quad (\text{A.8})$$

Averaging (A.7) over x gives

$$\begin{aligned} & \epsilon^6 \bar{\psi}_{\eta\eta\tau} + \epsilon^3 R \overline{\sin x \psi}_{\eta\eta\eta} + \epsilon^3 \overline{(\psi_x \psi_\eta)}_{\eta\eta} + \epsilon^6 \beta \bar{\psi}_\xi \\ & - \beta \alpha_5 \epsilon^6 \bar{\psi}_\eta = \epsilon^4 \bar{\psi}_{\eta\eta\eta\eta} - \epsilon^6 \mu_4 \bar{\psi}_{\eta\eta} + O(\epsilon^7). \end{aligned} \quad (\text{A.9})$$

Equation (A.9) is the basis of the weakly nonlinear description developed by Sivashinsky (1985).

We need also to expand u and β in powers of ϵ :

$$\begin{aligned} \mathcal{U} &= \mathcal{U}_0 + \epsilon \mathcal{U}_1 + \epsilon^2 \mathcal{U}_2 + \dots \\ \beta &= \beta_0 + \epsilon \beta_1 + \epsilon^2 \beta_2 + \dots \end{aligned} \quad (\text{A.10a, b})$$

Now we substitute

$$\psi = \psi_0 + \epsilon \psi_1 + \epsilon^2 \psi_2 + \dots \quad (\text{A.10c})$$

into (A.7). The leading order terms are

$$\mathcal{L}\psi_0 = 0, \quad (\text{A.11a})$$

where \mathcal{L} is the differential operator defined by

$$\mathcal{L}f = f_{xxxx} - \mathcal{U}_0 f_{xxx} - \beta_0 f_x. \quad (\text{A.11b})$$

Equation (A.11a) is solved by taking

$$\psi_0 = A(\xi, \eta, \tau). \quad (\text{A.12})$$

Collecting the terms of order ϵ from (A.7) gives

$$\mathcal{L}\psi_1 = R_c \sin x A_\eta. \quad (\text{A.13})$$

The solution of (A.13) is that

$$\psi_1 = (p \cos x + q \sin x) R_c A_\eta, \quad (\text{A.14a})$$

where

$$(p, q) \equiv \left[\frac{\beta_0 - \mathcal{U}_0}{1 + (\beta_0 - \mathcal{U}_0)^2}, \frac{1}{1 + (\beta_0 - \mathcal{U}_0)^2} \right]. \quad (\text{A.14b})$$

The critical Reynolds number is obtained by substituting (A.14) into the averaged potential vorticity equation (A.9) and collecting the terms which are of order ϵ^4 . The result is that

$$R_c^2 = 2[1 + (\beta_0 - \mathcal{U}_0)^2]. \quad (\text{A.15})$$

If $\beta_0 - \mathcal{U}_0 = 0$, then from (A.15) we recover the well-known result that the critical Reynolds number of a sinusoidal shear flow is $\sqrt{2}$ (Nepomnyashchy 1976; Sivashinsky 1985).

The order ϵ^2 terms from (A.7) give

$$\mathcal{L}\psi_2 = \mathcal{U}_1 \psi_{1xxx} - A_\eta \psi_{1xx} + \beta_1 \psi_{1x}. \quad (\text{A.16})$$

The solution of (A.16) is that

$$\psi_2 = R_c A_\eta (\beta_1 - \mathcal{U}_1 + A_\eta) [(q^2 - p^2) \cos x - 2pq \sin x]. \quad (\text{A.17})$$

Collecting the terms of order ϵ^5 from the averaged potential vorticity equation (A.9) forces us to make the coefficient of $\sin x$ in (A.17) zero. The alternative, admitting an evolution on the relatively fast timescale $\epsilon^3 t$, results in an amplitude equation that is an ill-posed nonlinear diffusion equation. The only way to avoid this is to remove the term proportional to $\sin x$ in (A.17) by taking $p = 0$. That is to say,

$$\mathcal{U}_0 = \beta_0. \quad (\text{A.18})$$

Adopting (A.18), we see from (A.14b) that $(p, q) = (0, 1)$. Thus, the expressions for ψ_1 in (A.14a) and ψ_2 in (A.17) simplify greatly. And from (A.15) we now obtain $R_c = \sqrt{2}$.

At order ϵ^3 in (A.7):

$$\begin{aligned} \mathcal{L}\psi_3 &= \mathcal{U}_0 \psi_{1\eta\eta x} + \mathcal{U}_1 \psi_{2xxx} + \mathcal{U}_2 \psi_{1xxx} + R_c \sin x A_{\eta\eta\eta} \\ &\quad + R_c \sin x A_\eta + \beta_1 \psi_{2x} + \beta_2 \psi_{1x} - A_\eta \psi_{2xxx} \\ &\quad - 2\psi_{1xxx\eta}. \end{aligned} \quad (\text{A.19})$$

The solution of (A.19) is that

$$\begin{aligned} \psi_3 &= R_c [\mathcal{U}_0 A_{\eta\eta\eta} + (\beta_2 - \mathcal{U}_2) A_\eta] \cos x \\ &\quad + R_c [-(\beta_1 - \mathcal{U}_1 + A_\eta)^2 A_\eta + 3A_{\eta\eta\eta} + A_\eta] \sin x. \end{aligned} \quad (\text{A.20})$$

Collecting the terms of order ϵ^6 from the averaged potential vorticity equation (A.9) we finally arrive at (2.12).

APPENDIX B

Weakly Nonlinear Analysis

We begin by rewriting (3.7b) in the form

$$\begin{aligned} U_\tau &= (\mu_c - \mu)U - \mathcal{M}U - 2\gamma(U^2)_{\eta\eta} \\ &\quad + \frac{2}{3}(U^3)_{\eta\eta}, \end{aligned} \quad (\text{B.1a})$$

where \mathcal{M} is the differential operator defined by

$$\mathcal{M}f = 3[\partial_\eta^2 + k_c^2]^2 f, \quad k_c^2(\gamma) = \frac{1}{6}(2 - \gamma^2). \quad (\text{B.1b})$$

In (B.1a), $\mu_c(\gamma) \equiv (2 - \gamma^2)/12$ is the critical value of the bottom drag; linear instability occurs if $\mu_c - \mu > 0$, for which μ is below the solid curve in Fig. 2. We now develop the weakly nonlinear theory when the bottom drag μ differs by a small amount from the critical value for linear stability μ_c :

$$\mu = \mu_c - \delta^2 \mu_2 - \delta^4 \mu_4, \quad (\text{B.2})$$

where δ is a small parameter. We introduce the slow timescales $T_2 \equiv \delta^2 \tau$ and $T_4 \equiv \delta^4 \tau$ and the amplitude expansion so that

$$\begin{aligned} U &= \delta U_1 + \delta^2 U_2 + \delta^3 U_3 + \dots, \\ \partial_\tau &= \delta^2 \partial_{T_2} + \delta^4 \partial_{T_4}. \end{aligned} \quad (\text{B.3})$$

Using (B.2) and (B.3) in (B.1), we have at order δ

$$\mathcal{M}U_1 = 0. \quad (\text{B.4})$$

We solve (B.4) with

$$U_1 = u(T_2, T_4) \exp(ik_c \eta) + (\text{c.c.}) \quad (\text{B.5})$$

At order δ^2 we get

$$\mathcal{M}U_2 = -2\gamma(U_1^2)_{\eta\eta}. \quad (\text{B.6})$$

Solving (B.6) gives U_2 :

$$U_2 = f_2 u^2 \exp(2ik_c \eta) + (\text{c.c.}),$$

$$f_2(\gamma) \equiv \frac{8}{27} \frac{\gamma}{2 - \gamma^2}. \quad (\text{B.7})$$

At order δ^3 we have

$$\begin{aligned} \mathcal{M}U_3 &= -U_{1T_2} + \mu_2 U_1 - 4\gamma(U_1 U_2)_{\eta\eta} \\ &\quad + \frac{2}{3}(U_1^3)_{\eta\eta}. \end{aligned} \quad (\text{B.8})$$

From the solvability condition of (B.8) we obtain the amplitude equation (3.10).

The solution of (B.8) is then given by

$$\begin{aligned} U_3 &= f_3 u^3 \exp(3ik_c \eta) + (\text{c.c.}), \\ f_3(\gamma) &\equiv \frac{1}{16} \frac{35\gamma^2 - 6}{(2 - \gamma^2)^2}. \end{aligned} \quad (\text{B.9})$$

The terms of order δ^4 give

$$\begin{aligned} \mathcal{M}U_4 &= -U_{2T_2} + \mu_2 U_2 - 2\gamma(U_2^2)_{\eta\eta} \\ &\quad - 4\gamma(U_1 U_3)_{\eta\eta} + 2(U_1^2 U_2)_{\eta\eta}, \end{aligned} \quad (\text{B.10})$$

the solution of which is

$$\begin{aligned} U_4 &= (f_4^{(1)}\mu_2 u^2 + f_4^{(2)}|u|^2 u^2) \exp(2ik_c \eta) \\ &\quad + f_4^{(3)}u^4 \exp(4ik_c \eta) + (\text{c.c.}), \end{aligned} \quad (\text{B.11a})$$

where the various coefficients are given by

$$\begin{aligned} f_4^{(1)}(\gamma) &\equiv \frac{64}{27} \frac{\gamma}{(2 - \gamma^2)^3}, \\ f_4^{(2)}(\gamma) &\equiv \frac{2\gamma}{729} \frac{2515\gamma^2 - 3942}{(2 - \gamma^2)^3}, \\ f_4^{(3)}(\gamma) &\equiv \frac{8\gamma}{3645} \frac{1207\gamma^2 - 558}{(2 - \gamma^2)^3}. \end{aligned} \quad (\text{B.11b})$$

Finally, at order δ^5 , one has

$$\begin{aligned} \mathcal{M}U_5 &= -U_{1T_4} - U_{3T_2} + \mu_2 U_3 + \mu_4 U_1 - 4\gamma(U_2 U_3)_{\eta\eta} \\ &\quad - 4\gamma(U_1 U_4)_{\eta\eta} + 2(U_1 U_2^2)_{\eta\eta} + 2(U_1^2 U_3)_{\eta\eta}. \end{aligned} \quad (\text{B.12})$$

The solvability condition produces a second amplitude equation for $u(T_2, T_4)$,

$$u_{T_4} = \mu_4 u - 4\gamma k_c^2 f_4^{(1)} \mu_2 |u|^2 u - h|u|^4 u, \quad (\text{B.13a})$$

where h has a rather awkward expression,

$$h(\gamma) \equiv \frac{350923\gamma^4 - 470700\gamma^2 + 8748}{34992(2 - \gamma^2)^2}. \quad (\text{B.13b})$$

Now we reconstitute the expansion by writing $u_\tau = \delta^2 u_{T_2} + \delta^4 u_{T_4}$; from (3.10) and (B.13) we get

$$\begin{aligned} u_\tau &= (\delta^2 \mu_2 + \delta^4 \mu_4)u - (\delta^2 \ell + \delta^4 4\gamma k_c^2 f_4^{(1)} \mu_2) |u|^2 u \\ &\quad - \delta^4 h|u|^4 u. \end{aligned} \quad (\text{B.14})$$

If we now set $\mu_2 = 0$ and $\gamma = \gamma_* + \delta^2 \gamma_2$ we obtain the equation

$$u_\tau = \delta^4 [\mu_4 u - \gamma_2 \ell_\gamma(\gamma_*) |u|^2 u - 1.5278 |u|^4 u], \quad (\text{B.15})$$

where ℓ_γ is the derivative of ℓ with respect to γ and $\ell_\gamma(\gamma_*) \approx -2.012 < 0$. This last equation is equivalent to (3.11).

REFERENCES

- Balmforth, N. J., 1995: Solitary waves and homoclinic orbits. *Annu. Rev. Fluid Mech.*, **27**, 335–373.
- Chapman, C. J., and M. R. E. Proctor, 1980: Nonlinear Rayleigh-Bénard convection with poorly conducting boundaries. *J. Fluid Mech.*, **101**, 759–782.
- Fraerman, A. A., A. S. Mel'nikov, I. M. Nefedov, I. A. Shereshevskii, and A. V. Shapiro, 1997: Nonlinear relaxation dynamics in decomposing alloys: One-dimensional Cahn-Hilliard model. *Phys. Rev. B*, **55**, 6316–6323.
- Frisch, U., B. Legras, and B. Villone, 1996: Large-scale Kolmogorov flow on the beta-plane and resonant wave interactions. *Physica D*, **94**, 36–56.
- Gill, A. E., 1974: The stability of planetary waves on an infinite beta-plane. *Geophys. Fluid Dyn.*, **6**, 29–47.
- Huang, H. P., and A. Robinson, 1998: Two-dimensional turbulence and persistent zonal jets in a global barotropic model. *J. Atmos. Sci.*, **55**, 611–632.
- Kawasaki, K., and T. Ohta, 1982: Kink dynamics in one-dimensional nonlinear systems. *Physica*, **116A**, 573–593.
- Lorenz, E. N., 1972: Barotropic instability of Rossby wave motion. *J. Atmos. Sci.*, **29**, 258–269.
- Meshalkin, L. D., and I. G. Sinai, 1961: Investigation of the stability of a stationary solution of a system of equations for the plane movement of an incompressible viscous fluid. *Appl. Math. Mech.*, **24**, 1700–1705.
- Nepomnyashchy, A. A., 1976: On the stability of the secondary flow of a viscous fluid in an infinite domain. *Appl. Math. Mech.*, **40**, 836–841.
- Nozawa, T., and S. Yoden, 1997: Formation of zonal band structures in forced two-dimensional turbulence on a rotating sphere. *Phys. Fluids*, **9**, 2081–2093.
- Panetta, R. L., 1993: Zonal jets in wide baroclinically unstable regions: Persistence and scale selection. *J. Atmos. Sci.*, **50**, 2073–2106.
- Rhines, P. B., 1975: Waves and turbulence on a β -plane. *J. Fluid Mech.*, **69**, 417–443.
- , 1994: Jets. *Chaos*, **4**, 313–339.
- Salmon, R., 1980: Baroclinic instability and geostrophic turbulence. *Geophys. Astrophys. Fluid Dyn.*, **15**, 167–211.
- Sivashinsky, G. I., 1985: Weak turbulence in periodic flows. *Physica D*, **17**, 243–255.
- Thual, O., and S. Fauve, 1988: Localized structures generated by subcritical instabilities. *J. Phys.*, **49**, 1829–1833.
- Vallis, G. K., and M. Maltred, 1993: Generation of mean flow and jets on a beta-plane and over topography. *J. Phys. Oceanogr.*, **23**, 1346–1362.
- Williams, G. P., 1978: Planetary circulations: I. Barotropic representation of Jovian and terrestrial turbulence. *J. Atmos. Sci.*, **35**, 1399–1426.